Supplemental Materials for
A magnetic Weyl semimetallic phase in thin films of Eu$_2$Ir$_2$O$_7$

Xiaoran Liu*, Shiang Fang*, Yixing Fu, Wenbo Ge, Mikhail Kareev, Jong-Woo Kim, Yongseong Choi, Evguenia Karapetrova, Qinghua Zhang, Lin Gu, Eun-Sang Choi, Fangdi Wen, Justin H. Wilson, Gilberto Fabbris, Philip J. Ryan, John Freeland, Daniel Haskel, Weida Wu, J. H. Pixley, Jak Chakhalian

*Corresponding author
Email: xiaoran.liu@rutgers.edu; shiangfang913@gmail.com

This PDF includes:

Sections S1 to S6

Figs. S1 to S20

Table S1

References and Notes

Section S1   Film characterizations

The (111) oriented $Eu_2Ir_2O_7$ thin films were grown on 5×5 mm^2 (111) yttria-doped ZrO_2 (YSZ) substrates by the *in-situ* solid phase epitaxy method (*1*). Ir-rich phase-mixed ceramic target (Eu:Ir = 1:3) was ablated using a KrF excimer laser (λ = 248 nm, energy density $\sim$ 6 J/cm^2) with a repetition rate of 10 Hz. The deposition was carried out at a substrate temperature of 450 °C, under 100 mTorr atmosphere of mixture of Ar and O_2 gases (partial pressure ratio, Ar:O_2 = 10:1). Amorphous film with the proper stoichiometry was obtained from this stage. The film was post-annealed inside the chamber at 950 °C, under 500 Torr atmosphere of pure O_2 for 30 min, and then cooled down to room temperature. High-quality crystalline and single phase (111) $Eu_2Ir_2O_7$ thin film was eventually achieved.

The scanning transmission electron microscopy (STEM) measurements were carried out using a spherical aberration-corrected JEM-ARM200F, operated at 200 kV. The high-angle annular dark-field (HAADF) imaging was taken using the collection semi-angle of about 70-250 mrad.

In this section, more information about the morphological characterizations of the film are exhibited in Fig. **S2**. As shown in Fig. **S2**A, the (111) diffraction of EIO is clearly observed with distinct interference fringes, which indicates the establishment of film with high crystallization and well-defined layered structure. Assuming the cubic symmetry is preserved in film, the calculated lattice parameter is $\sim$10.26 Å, very close to the value (a $\sim$10.27Å) of bulk EIO (*2*). And the calculated film thickness is around 40 nm. In addition, as shown in Fig. **S2**B, the rocking curve scan around the EIO (444) diffraction yields a full-width-at-half-maximum (FWHM) of 0.12°, corresponding to a rough estimation of the lateral coherence length $\geq$0.6 μm.

The film-substrate epitaxial relationship and the strain status were further investigated by az-

imuthal ϕ-scan and reciprocal space mappings. As displayed in Fig. **S2**C, the ϕ-scan of the EIO $(2\bar{2}2)$ diffraction (in blue) exhibits the same three-fold symmetry as the YSZ substrate's $(1\bar{1}1)$ diffraction, signifying that the film contains neither mis-oriented domains nor stacking faults. Moreover, on the reciprocal space mappings (Fig. **S2**D) in the vicinity of YSZ (331) diffraction, the EIO (662) diffraction is clearly observed, confirming the expected film-substrate epitaxial relationship, i.e., EIO $(111)[11\bar{2}]$ // YSZ$(111)[11\bar{2}]$. Moreover, the EIO (662) diffraction locates not along the direction with the same Q_X as substrate, but along the radial direction relative to the origin of the reciprocal space, and the calculated lattice parameter from EIO (662) is also $\sim$10.26 Å. These combined results confirm a nearly complete relaxation of the strain.

To further obtain a microscopic view of the film structure and crystallization, a scanning transmission electron microscopy high-angle annular dark-field (STEM-HAADF) image of the (111) EIO film grown on YSZ substrate is shown in Fig. **S2**E. The cross-sectional image was projected along the [111] and $[1\bar{1}0]$ directions. It is confirmed that the EIO film is coherently established on the YSZ substrate, and the film-substrate interface is sharp with no blurry area nor buffered layer.
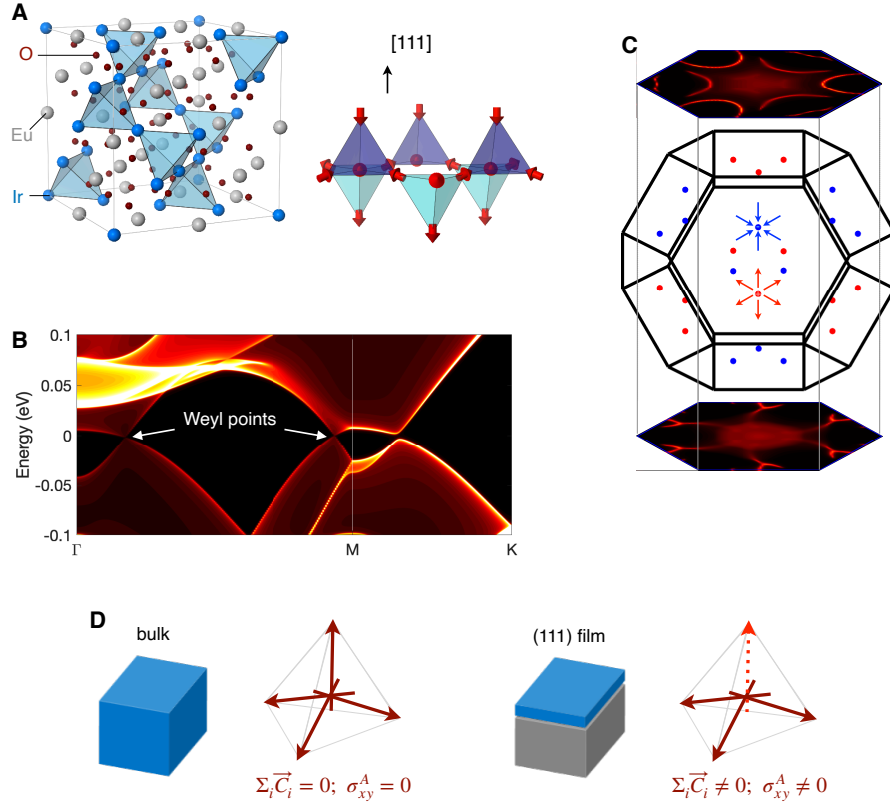
Fig. S1: From bulk $Eu_2Ir_2O_7$ crystals to high-quality (111) thin films. **(A)** Unit cell of $Eu_2Ir_2O_7$ with the Ir corner-sharing tetrahedral framework (top), and the "all-in-all-out" antiferromagnetic order (bottom). **(B)** Spectral weight of the electronic bands near the Fermi level, along with the Weyl points in the WSM. **(C)** 24 Weyl points in bulk Brillouin zone (BZ), where the red/blue color denotes the $\chi = \pm 1$ chirality from the Berry curvature flux. The nontrivial topology leads to Fermi arc surface states when the bulk crystal is cleaved. The top (bottom) projections are the spectral plots in the surface BZ cleaved at the kagome (triangle) terminated atomic plane perpendicular to [111]. **(D)** Emergence of intrinsic anomalous Hall effect in (111) $Eu_2Ir_2O_7$ thin film as a result of broken cubic symmetry.

4
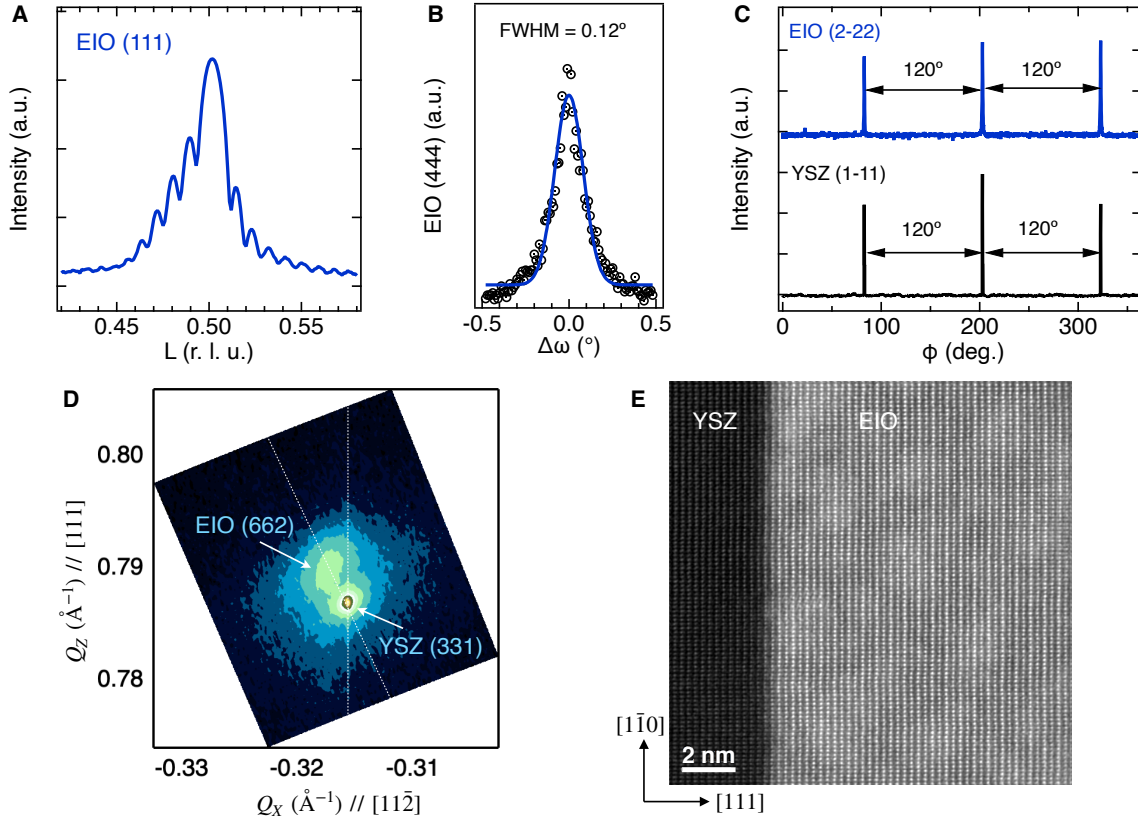
Fig. S2: **(A)** Coupled HKL-scan around the EIO (111) diffraction in the reciprocal lattice unit (r.l.u.) of YSZ substrate. **(B)** Rocking curve scan of the EIO (444) diffraction. The FWHM is around 0.12°. **(C)** Azimuthal ϕ-scans around the YSZ (1-11) and the EIO (2-22) diffraction, respectively. Both peaks exhibit the threefold symmetry. **(D)** Reciprocal space mappings around YSZ (331) diffraction. The EIO (662) diffraction is clearly observed along the radial direction in the reciprocal space. **(E)** STEM-HAADF cross-sectional imaging of the (111) EIO film on YSZ substrate.

# Section S2 Synchrotron-based x-ray scattering experiments

The synchrotron-based x-ray scattering experiments were carried out on beamline 6-ID-B and 33-BM-C of the Advanced Photon Source, Argonne National Laboratories. The geometry of experimental setup is illustrated in Fig. **S3**A. The (111) EIO film was mounted on the sample holder in a closed-cycle displex. The incident x-rays were linearly polarized perpendicular to the scattering plane (σ). The [110] axis of the film was aligned normal to the scattering plane. To further perform the polarization analysis at beamline 6-ID-B, a Pyrolytic graphite (001) crystal was used to analyze the polarization of the scattered x-rays (linear polarization σ perpendicular to the scattering plane; linear polarization π parallel to the scattering plane). The 2θ value of its (008) reflection is 82.452°, leading to a polarization purity of 98.3%. The intensity of scattering in different channels (σ-σ and σ-π) was recorded by rotating the detector about the scattered beam.

Section S2.1 Anisotropic tensor susceptibility scattering

In order to measure the space-group forbidden (0 0 4n+2) reflections at beamline 6-ID-B, the energy of the incident x-rays were tuned to the Ir L_3 absorption edge to trigger the resonant process. Polarization analysis was performed in these measurements. As shown in the main text Fig. 2(a), both the resonant magnetic scattering (RMS) and the anisotropic tensor susceptibility (ATS) scattering contribute to $Eu_2Ir_2O_7$ (0 0 10) reflection. However, unlike RMS, the ATS is resulted from the local trigonal distortion of the IrO_6 octahedra, which leads to the anisotropic nature of d orbital shapes and charge distribution at the Ir sites. Thus, it is a Templeton scattering and dominant in the σ-σ channel (*3–5*). Here, in Fig. **S3**, we show the detailed results of the EIO (0 0 10) reflection recorded in the σ-σ channel, with the energy of incident x-rays set at 11.22 keV.

A clear peak is observed during the L scan (in reciprocal lattice unit of the YSZ sub-
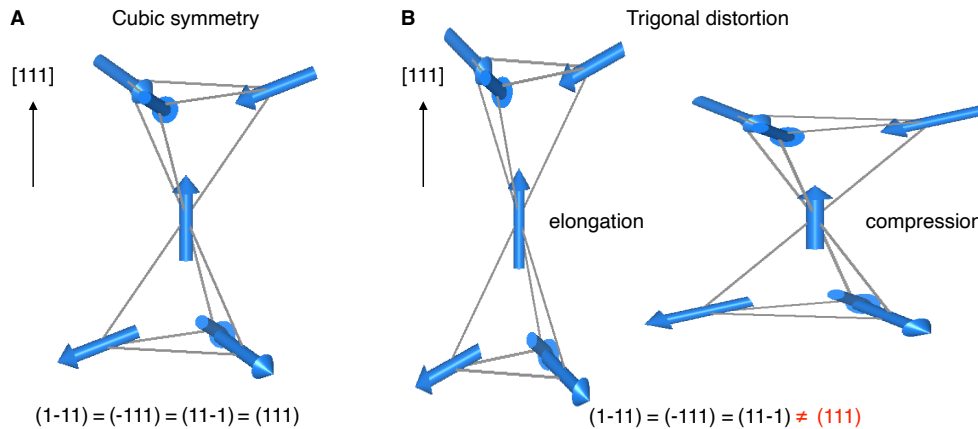
strate), which however, doesn't vary at temperatures above and below the magnetic transition (Fig. **S3**B). This is more evident from its integrated intensity as a function of temperature (Fig. **S3**C), which exhibits an overall temperature independent feature. These data are consistent with previous results from $Eu_2Ir_2O_7$ bulk, corroborating it non-magnetic in origin (*5*).
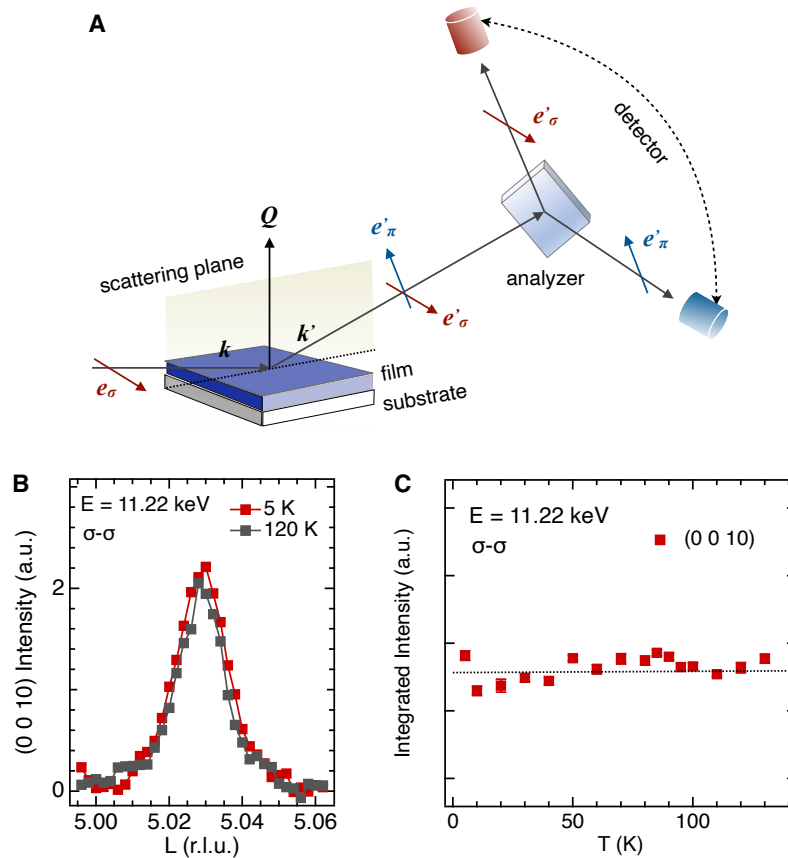
Fig. S3: **(A)** Illustration of the experimental geometry. **(B)** L scans of (0 0 10) reflection of the $Eu_2Ir_2O_7$ thin film in σ-σ channel above and below the magnetic transition, with incident energy fixed at 11.22 keV. **(C)** Variation of the ATS (0 0 10) integrated intensity (over L) as a function of temperature. The lack of a distinct temperature dependence corroborates its nature of a Templeton reflection.

Section S2.2 Degree of trigonal distortion in $Eu_2Ir_2O_7$ thin film

In order to investigate the degree of trigonal lattice distortion in the film, we performed x-ray diffraction experiments on structurally allowed reflections at beamline 33-BM-C. No polarization analysis is needed in this case. The energy of incident x-rays were set at 16 keV, away from any absorption edge of the constituent element. The measurements were taken at 300 K. As illustrated in Fig. **S4**, within the cubic symmetry, the four reflections, (1-11), (-111), (11-1), and (111) are equivalent such that they have the same 2θ values in the diffraction measurements. However, if there is trigonal lattice distortion induced by strain (either elongation or compression) along the [111] direction, the (111) reflection will no longer be equivalent to the other three reflections, exhibiting a distinctly different 2θ value.

A   Cubic symmetry   **B**   Trigonal distortion

[111]   [111]

elongation   compression

(1-11) = (-111) = (11-1) = (111)   (1-11) = (-111) = (11-1) ≠ (111)

Fig. S4: **(A)** and **(B)** Schematic illustration of the possible trigonal lattice distortions relative to the cubic symmetry in the film, and the corresponding effects on the {111} reflections.

We measured the detailed 2θ values of those four reflections for both {111} and {333} families. As listed in Table **S1**, within the precision of experiments, the peak position of 2θ scan of each reflection is primarily the same, indicating the cubic symmetry is still preserved in the film. In fact, this is consistent with the results from reciprocal space mappings shown in previous section, demonstrating the epitaxial strain is nearly completely relaxed. As a result,

Table S1: 2θ values of the $\{111\}$ and $\{333\}$ reflections of $Eu_2Ir_2O_7$ thin film.

h	k	l	2θ (°)
1	1	1	7.497
1	-1	1	7.503
-1	1	1	7.497
1	1	-1	7.494
3	3	3	22.585
3	-3	3	22.591
-3	3	3	22.577
3	3	-3	22.602

the trigonal distortion, if any, is vanishingly small inside the film such that it is not the origin which can induce the observed anomalous Hall effect.

Section S3 Magneto-transport measurements

## Section S3.1 Detailed procedure of the magneto-transport measurements

The electrical transport measurements were performed in a 9-T physical property measurement system (PPMS, Quantum Design) with the 4-point contact method. The magnetic field was applied along the [111] direction, and the current was driven along the [$1\bar{1}0$] direction. In order to roughly estimate a putative gap from the $\rho(T)$ curve, the Arrhenius's relationship $\rho(T) = \rho(0)exp(E_a/k_BT)$ can be written such that the activation gap E_a is expressed as a function of temperature $E_a = (8.57meV) * ln[\rho(T)/\rho(0)]/(100/T - 1)$, as shown in the main text Figure 3(a) inset. The $\rho(0)$ is canceled by plugging in the minimal resistivity measured at 100 K, $\rho(100)$.

In the following, we emphasize the detailed procedures of our magneto-transport measurements and explain the underlying reasons. Below $\sim$95K, the saturation field (H_S) of the loop of anomalous Hall effect (AHE) exceeds the maximum field of a standard 9-T PPMS system, which can be applied to the measurements. As a result, simply sweeping the field at a fixed temperature below 95K can only lead to an undesired minor AHE loop without saturating the sample and quenching the magnetic domains. This would further give rise to ambiguous result when symmetrization and anti-symmetrization analyses are applied to obtain the pure longitudinal and transverse resistivity. In order to trace the correct major AHE loop and to identify the coercivity and saturation properly, one has to quench the domains by thermal heating and cooling. Specifically, the procedures are depicted in Fig. **S5**A.

The saturation field H_S and coercivity H_C can be identified from the AHE loop, by subtracting the linear ordinary Hall contribution from the total Hall response. The corresponding H_C and H_S are shown in Fig. **S5**B. Note that, H_C and H_S is directly visible from the AHE loop only when they are smaller than 9T. The H_C and H_S above 9T are obtained by either fitting the

AHE loop or extrapolation. As shown in Fig. **S5**B, decreasing the temperature, both H_C and H_S increase rapidly and gigantically. A simple linear fit leads to H_C (H_S) $\sim$84 T (144 T) at 0 K!

Temperature dependences of the AHE-related parameters are shown in Fig. **S6**.
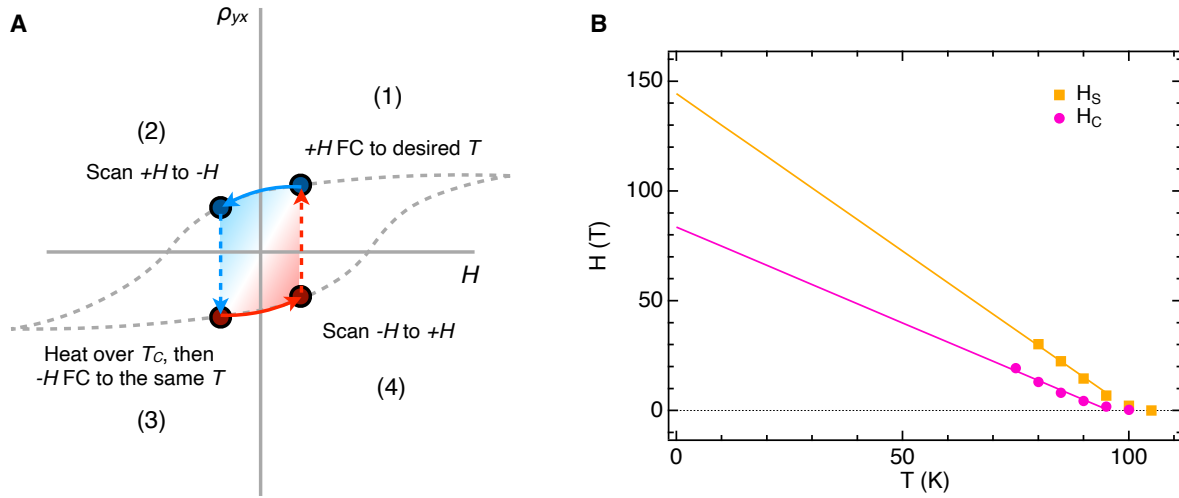
Fig. S5: **(A)** Schematics of the measuring procedure. (1), the sample is field cooled (FC) from 130 K to some desired temperate under +9 T magnetic field. (2), one branch of the major loop (blue) is traced by sweeping the field from +9 to -9 T. (3), sample is heated over the transition to 130 K and then FC back to the same desired temperature. (4), the other branching of the major loop (red) is now accessible by sweeping the field from -9 to +9 T. Since H_C and H_S are extremely large at lower temperatures, only the middle region of the major loop (shaded area) can be traced. **(B)** H_C and H_S at different temperatures. Above 95 K, both can be identified from the AHE loops. Below 95 K, the AHE loop is fitted by rescaling the AHE loop to extrapolate H_C and H_S. A simple linear fit leads to H_C (H_S) $\sim$84 T (144 T) at 0 K.
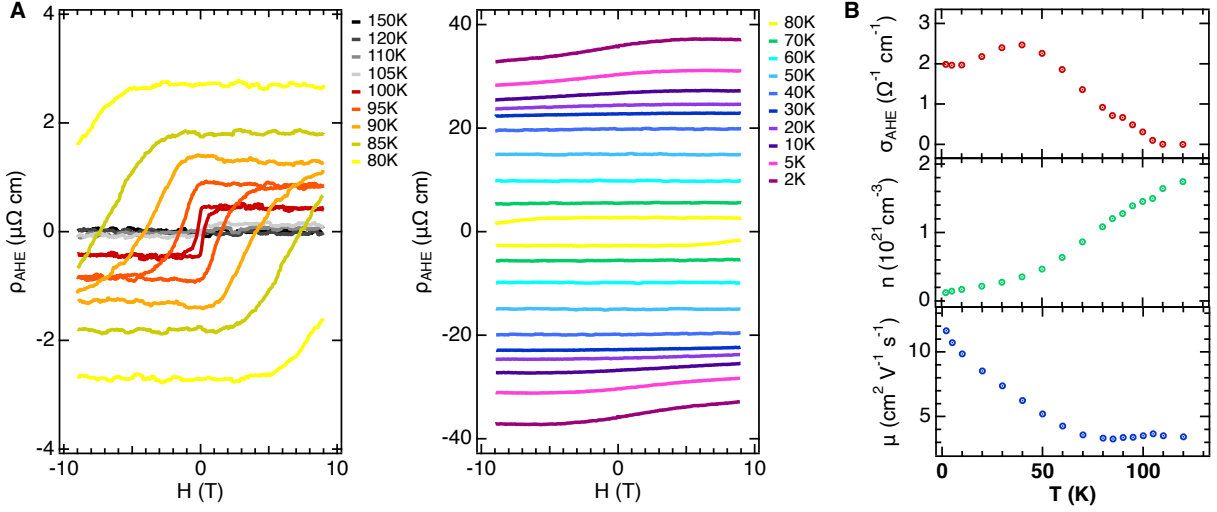
Fig. S6: **(A)** Comprehensive exhibition of the evolution of the anomalous Hall resistivity from 150 K to 80 K (left) and from 80 K to 2 K (right). **(B)** Temperature dependence of the calculated anomalous Hall conductivity σ_{AHE}, carrier density n, and mobility μ.

Section S3.2   High-field magneto-transport

High-field magneto-transport experiments up to 18 T were carried out in the National High Magnetic Field Laboratory in Tallahassee. Following the same procedures described in previous section, we measure both the longitudinal (R_{xx}) and transverse (R_{yx}) magnetoresistance at 85 K and 1.4 K, as shown in Fig. **S7**. At 85 K, only an incomplete hysteresis loop was previously obtained using a standard 9 T PPMS system, as seen in Fig. **S6**. However, with a 18 T magnet, the complete hysteresis loop is now accessible, exhibiting the magnetic coercivity H_C and saturation H_S about 7 T and 15 T, respectively. On the other hand, however, due to gigantic H_C and H_S at 1.4 K, we can only reach the small portion in the middle of the loop with no indication of H_C and H_S. These results clearly demonstrate the rapid and profound evolution of H_C and H_S at lower temperatures due to the formation of all-in-all-out (or all-out-all-in) magnetic octupole domains. Once established, the domains can hardly be quenched by direct sweeping of external magnetic field.
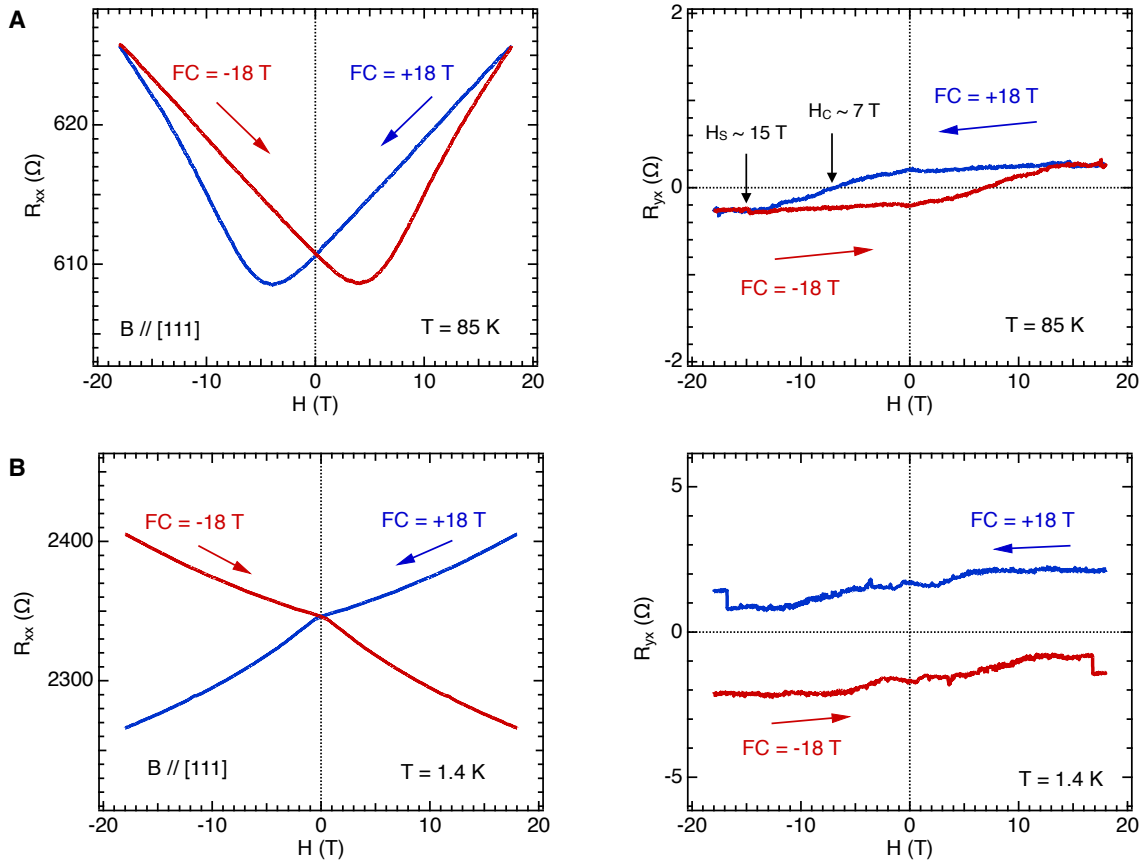
Fig. S7: **(A)** and **(B)** Longitudinal (left) and transverse (right) magnetoresistance up to 18 T of the $Eu_2Ir_2O_7$ thin film at 85 K and 1.4 K, respectively.

Section S4   Magnetization along the [111] direction

The x-ray magnetic circular dichroism experiments were performed at beamline 4-ID-D of the Advanced Photon Source at Argonne National Laboratory. X-ray absorption spectra around Ir L_3 and L_2 edges were collected with left- and right- circularly polarized beams at nearly normal incidence (k // [111]) to obtain the x-ray magnetic circular dichroism (XMCD). To exclude any artifact, XMCD was measured with magnetic field applied along and opposite the x-ray propagation direction. In case of large magnetic coercivity, the measurements were conducted in two ways for comparison. (1) XMCD was recorded after sample was +6 T field cooled to 4 K; then sample was heated to 150 K (to quench any magnetic ordering) and cooled back to 4 K with -6 T field, after which XMCD was recorded. (2) XMCD was recorded after sample was +6 T field cooled to 4 K. Then the magnetic field was directly swept to -6 T at 4 K, after which XMCD was recorded. The spectra obtained in both ways are almost identical.

In order to verify the octupole contribution to the dichroic signals, we have performed the XMCD experiments in two different approaches. In the first approach, following the conventional procedure, the film was zero-field cooled down to 4 K before recording the XMCD signal in ±6 T field. In this situation, the sample is of multi-domains, with approximately equal number of AIAO and AOAI domains. In the second approach, the film was ±6 T field cooled down to 4 K before recording the XMCD signal, respectively. In this situation, the sample is always of single-domain. However, the XMCD signals obtained from both approaches are practically the same. Thus, the octupole has a negligible contribution to the observed XMCD signal.

Sum rules (*6, 7*) were applied on the Ir $L_{3,2}$ x-ray absorption spectra (XAS) and magnetic circular dichroism (XMCD) to deduce the averaged net magnetic moment per Ir^{4+} ion ($5d^5$) of our (111) $Eu_2Ir_2O_7$ thin film. Data were collected at 4 K using the fluorescence detection mode, under an applied field of 6 T normal to the sample surface.

The orbital magnetic moment is directly calculated from the orbital sum rule: $m_o = -2(A + B)/3C \cdot (10 - N_d)$, where A, B, and C represent the integrated intensity of Ir L_3 XMCD, L_2 XMCD, and Ir XAS white line, respectively (*8, 9*). And N_d is the number of Ir^{4+} $5d$ electrons. This leads to $m_o \approx 0.006(2)$ [μ_B/Ir]. The spin magnetic moment is calculated from the spin sum rule: $m_s = -(A - 2B)/C \cdot (10 - N_d) \cdot (1 + 7\langle T_z \rangle/2\langle S_z \rangle)^{-1}$, in which $\langle S_z \rangle$ and $\langle T_z \rangle$ refer to the spin angular momentum and the intra-atomic dipole term, respectively (*8, 9*). Here we refer to the estimation of $\langle T_z \rangle \approx 0.2\langle S_z \rangle$ from configuration interaction calculations (*10*). This leads to $m_s \approx 0.003(4)$ [μ_B/Ir]. As a consequence, the averaged net moment per Ir ion is obtained as $m_{net} = m_o + m_s \approx 0.009(6)$ [μ_B/Ir] under 6 T magnetic field. We note the measured quantity is not the *local* magnetic moment per Ir ion, which is $\sim$0.33 μ_B estimated from the J_{eff} = 1/2 ground state configuration (*11*). Such a small net moment is likely a result of the canting of the Ir spins by large magnetic field away from the perfect all-in-all-out antiferromagnetic ordering, which is consistent with the interpretation based on high-field magneto-transport results.
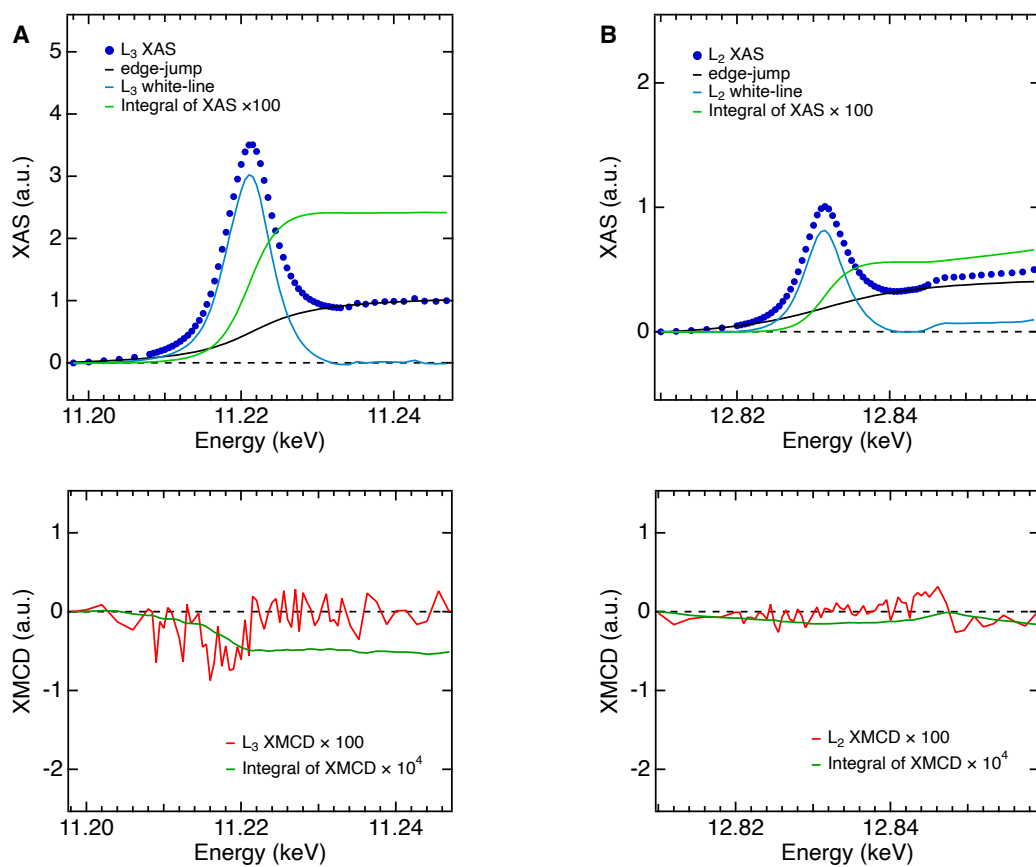
Fig. S8: **(A)** and **(B)** XMCD sum rules analyses on Ir $L_{3,2}$ XAS and XMCD spectra. The corresponding integrated intensity is exhibited in green line on each figure.

# Section S5 First-principles electronic structure modeling

We have performed first principles density functional theory calculations to investigate the electronic properties of $Eu_2Ir_2O_7$, implemented in the Vienna ab initio simulation package (VASP) [12,13]. For the pseudopotential formalism, the Projector Augmented-Wave method [14] was used with Perdew-Burke-Ernzerhof (PBE) [15] parametrized exchange-correlation energy functional. We have also used Eu 3+ pseudopotential for Eu atoms, consistent with the valency state probed experimentally. We further include an adjustable Hubbard U_{Ir} parameter on Ir atoms prescribed by the rotationally invariant approach to the LSDA+U [16]. The electronic ground states were converged with an energy cutoff 450 eV, a Γ-centered $9 \times 9 \times 9$ Monkhorst-Pack k-mesh grid, relativistic spin-orbit coupling terms, and AIAO magnetic structure.

With the converged electronic ground state, we construct the electronic structure models by employing the Wannier transformation [17] implemented in Wannier90 code [18, 19]. To project out the low energy degrees of freedom, we include only the Ir $t2g$ orbitals defined by surrounding oxygen octahedra and both spin degrees of freedom. Based on the Wannier transformation of periodic Bloch waves, we have derived the localized Wannier functions and the real space tight-binding Hamiltonians. Using WannierTools [20] code, the Weyl point locations can be efficiently identified. With these models generalized for the slab geometry, we compute the Berry curvature [21] and local Chern marker [22, 23] for the anomalous Hall response. Iterative Green's function methods [24] are used to derive the surface spectral functions in the extended semi-infinite geometry. To consider real system size and thickness scaling properties, we also perform large system simulations based on kernel polynomial method [25].

Section S5.1　Bulk electronic structure and phase diagram

To obtain the electronic properties of $Eu_2Ir_2O_7$, we have performed first principles density functional theory calculations, implemented in the Vienna ab initio simulation package (VASP) (*12, 13*).nd state electronic structure, LSDA+U (*16*) and spin-orbit coupling terms are included to account for the onsite Hubbard interactions and the magnetic structure. The AIAO magnetic structure is found to be stable with Hubbard interaction terms on Ir-d orbit To derive the self-consistent grouals (denoted as U_{Ir}) greater than U_{c1}, with varying magnetic moment magnitude as shown in Fig. 1(a) (main text). The electronic ground states are found to be in normal metal (NM), Weyl metal (WM), Weyl semi-metal (WSM), and anti-ferromagnetic insulator (AFI) phases at transitions $U_{c1} \sim 0.7$ eV, $U_{c2} \sim 1.05$ eV and $U_{c3} \sim 1.45$ eV. In the WM phase, there are 8 Weyl nodes near the Fermi level (see Sec. Section S6.2 below). However, there are parasitic metallic bands at the same Fermi energy which masks the distinguished Weyl semi-metal features, and hence it is called Weyl metal phase instead. For $U_{c2} < U_{Ir} < U_{c3}$, there are 24 Weyl points found near the Fermi level (see Supplementary Materials, Fig. **S1**(c)), which is the WSM phase we focus on here for the thin film. As demonstrated below, for most values of U_{Ir} in the WSM phase there is a very narrow gap in other parts of the band structure at the Fermi energy of the Weyl node, which can make a number of spectral probes look metallic. As U_{Ir} increases, the Weyl points annihilate and the electronic structure undergoes a WSM-to-AFI transition at around U_{c3}. More extended phase diagram discussions which are relevant for pyrochlore iridates are also investigated at various levels of theoretical treatment to treat electron correlations beyond the mean field DFT+U approach here (*26–31*). While interaction effects could greatly renormalize the quasi-particle properties, the phase diagram obtained in this work agrees qualitatively with the recent cluster dynamical mean field theory calculations (*32, 33*). As our main aim is to theoretically understand the origin of the AHC observed in experiment and its nature across the phase diagram, modeling at the DFT+U level is sufficient. It will be

interesting in future work to investigate the AHC treating interactions at a more accurate level.
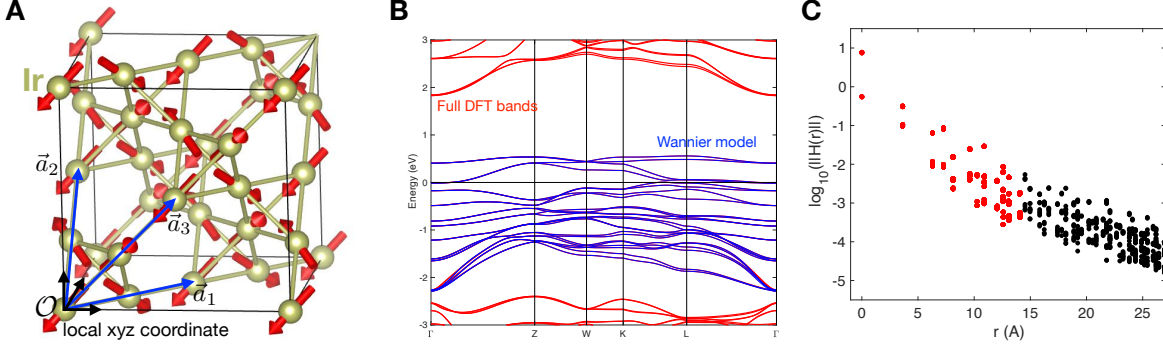
Fig. S9: **(A)** Ir atoms form a pyrochlore lattice structure. The primitive cell lattice vectors are denoted by blue arrows. The conventional cubic unit cell is also shown, which defines the local xyz coordinate frame at $\mathcal{O}$. In the Wannier projection, $t2g$ orbitals (d_{xz}, d_{yz}, d_{xy}) are defined in the local frame at the Ir site. **(B)** The reconstructed Wannier bands (blue) capture well the full DFT bands (red) near the Fermi level. **(C)** At U = 1.4 eV, we analyze the pair coupling strength (in units of eV) versus pair distance r (Å). A distance cutoff (14.5 Å) for tight-binding coupling terms (red dots) are employed to truncate the full Wannier model.

Section S5.2 Wannier tight-binding modeling

To investigate the electronic structure based on these DFT results, we employed the Wannier transformation to derive effective tight-binding models (*17*), implemented in Wannier90 code (*18, 19*). To elaborate on the model construction, we start with the settings for the conventions of the modeling. In terms of the crystalline symmetry, the crystal has a space group SG227 ($Fd\bar{3}m$). The primitive vectors for the unit cell are $\vec{a}_1 = \frac{a_0}{\sqrt{2}}(\hat{x} + \hat{y})$, $\vec{a}_2 = \frac{a_0}{\sqrt{2}}(\hat{y} + \hat{z})$, $\vec{a}_3 = \frac{a_0}{\sqrt{2}}(\hat{x} + \hat{z})$ with $a_0 \sim 7.262$ Å. The crystal structure is shown in Fig. **S9**A and the four Ir atoms are located at 0, $\vec{a}_1/2$, $\vec{a}_2/2$ and $\vec{a}_3/2$ respectively.

In the Wannier transformation, only the Ir t_{2g} orbitals are used to perform the low-energy model projections. (Full projection with all the Ir d orbitals can be carried out as well, but the e_g bands are much higher in energy hence irrelevant to the low-energy effective models. This greatly simplifies the slab calculations later allowing us to reach large system sizes.) In

19

this crystal convention, these t_{2g} states are the local atomic d_{xy}, d_{xz} and d_{yz} orbitals defined by the surrounding oxygen octahedra (see Fig. **S9**A for the crystal structure and local coordinate frame), with the spin degrees of freedoms included to capture the magnetic structure. In a unit cell, there are a total of 24 Wannier basis states. With the Wannier transformation, one can derive the real space tight-binding Hamiltonian. This effective Hamiltonian can be used to reconstruct the low-energy bands efficiently when comparing to the full DFT computations as shown in Fig. **S9**B. By using WannierTools (*20*), one could analyze the electronic structure properties such as locating Weyl nodes in the BZ efficiently.

To extract more details on the projected Wannier Hamiltonian, we define H_{n_1,n_2,n_3} as the hopping matrix from the central unit ($\vec{R} = 0$) to a unit at $\vec{R} = n_1\vec{a}_1 + n_2\vec{a}_2 + n_3\vec{a}_3$, a 24×24 matrix. In momentum space, the total Hamiltonian can be written as

$$H(\vec{k}) = \sum_{n_1,n_2,n_3} H_{n_1,n_2,n_3} e^{-i\vec{k}\cdot(n_1\vec{a}_1+n_2\vec{a}_2+n_3\vec{a}_3)}, \tag{1}$$

With this effective Hamiltonian, one can efficiently derive the electronic structure and investigate the band structure, density of states, Berry curvature (*21*), and transport properties, all of which we compute numerically. For smaller systems, we use exact diagonalization, whereas for larger system sizes we employ the kernel polynomial method (KPM) (*25*) which will be introduced later.

Regarding AHE, due to the cubic symmetry of the bulk crystal, the integrated Berry curvature of the filled bands (anomalous Hall response) has to vanish *exactly* in all directions. Therefore the cubic symmetry has to be broken in order to generate a non-zero AHE signal. The thin film naturally breaks the symmetry by picking a preferred 111 axis normal to the termination surface, and we will discuss the numerical modeling for thin film slabs in the next section.

## Section S5.3 Slab geometry with finite thickness

Given the bulk tight-binding Hamiltonian as derived above, one can construct a finite slab model to simulate the thin film geometry and the surface effects. In the pyrochlore iridate structure, one can identify the geometry of stacked Ir kagome and triangular lattices along the $[111]$ direction (shown in main text). These planar structures are normal to the $\hat{x} + \hat{y} + \hat{z}$ vector. Each repeated unit consists of both kagome and triangular layers. Most importantly, the thin films experimentally studied here are grown along this direction. By reading off the bulk Hamiltonian terms, one can derive the tight-binding model for a slab geometry. To be specific, we classify the terms from the bulk Hamiltonian H_{n_1,n_2,n_3} by the sum of the indices $n' = n_1 + n_2 + n_3$ and define

$$T_n(\vec{k}) = \sum_{n_1+n_2+n_3=n} H_{n_1,n_2,n_3} e^{-i\vec{k}\cdot(n_1\vec{a}_1+n_2\vec{a}_2+n_3\vec{a}_3)} \tag{2}$$

where $\vec{k} \perp \hat{x} + \hat{y} + \hat{z}$ describes the two-dimensional crystal momentum of the slab geometry. Intuitively, $T_n(\vec{k})$ describes couplings from the 0-th layer unit to the n-th layer unit. Note that one unit here contains both the kagome and triangular Ir lattice sublayers. Numerically, one can truncate at $T_{\pm2}(\vec{k})$ due to the vanishing couplings to further layer units, in the following we used a cutoff of $\sim 14.5\text{Å}$ for the coupling pair distance. In Fig.**S9**C, we show the pair coupling strength versus the pair distance, and the truncated terms are at most on the order of meV. In a slab geometry with stacks of N units (each unit has a triangle sheet and a kagome sheet, and a total of 24 basis states), with index $i = 1$ to N, the total Hamiltonian can be modeled as

$$H_{i,i}(\vec{k}) = T_0(\vec{k}), H_{i\pm1,i}(\vec{k}) = T_{\pm1}(\vec{k}), H_{i\pm2,i}(\vec{k}) = T_{\pm2}(\vec{k}) \tag{3}$$

and $H_{i,j}(\vec{k}) = 0$ for the rest of the terms. In the modeling, the two surfaces are terminated with a kagome and a triangular lattice respectively. We use this geometry to retain the stoichiometry and vanishing net magnetic moment with perfect AIAO magnetic ordering. However, by removing the additional degrees of freedom in the basis, one can control which type of sublayer
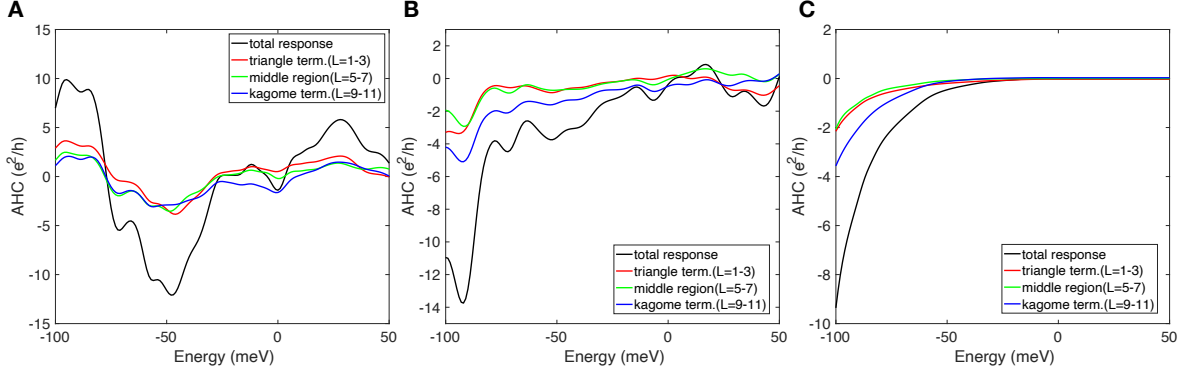
Fig. S10: The layer-resolved AHC as function of energy for a 11-layer slab with **(A)** $U = 1.0$ eV (WM) **(B)** $U = 1.3$ eV (WSM) **(C)** $U = 1.5$ eV (AFI). The total AHC response (black) is compared with the partial contributions from near triangle termination surface (red for layer index 1-3), middle region (green for layer index 5-7) and triangle termination surface (blue for layer index 9-11)

to appear at the surface termination. Later in the last section, we will also present results for simulations based on the slabs with identical termination surfaces on both sides, which carry a net magnetic moment.

Section S5.4   Computational approaches to the density of states, transport, Berry curvature, and layer resolved quantities

Section S5.4.1   Exact Diagonalization

For the AHE, in contrast to the bulk case above, here we arrive at the non-zero anomalous Hall values in general for the thin film slabs due to the reduced symmetries present in the geometry, especially the removal of cubic symmetry. Intuitively, such Hall response should originate near the surface due to the reduced symmetries compared to the bulk crystal. First of all, we numerically compute the total anomalous Hall conductance for a thin slab and find non-zero responses as presented. The numerical implementation is based on Ref. (*21*) by capturing the Berry flux or the Berry phase in traversing small plaquettes in momentum space. A temperature smearing with $k_B T = 2$ meV is used to obtain smoother results.

To derive the layer resolved Hall responses, one can employ the "Chern marker" calculations in Ref. (*22, 23*) which computes the spatially resolved anomalous Hall conductivity (AHC). In the main text, we show various signatures that imply the Hall response would come from the surface layers in contrast to the middle layers which approach to the vanishing bulk response for the thicker films. The layer-resolved anomalous Hall response applicable to the slab geometry is derived as (*23*)

$$g_{xy}^{(l)} = \left(\frac{e^2}{h}\right) \int_{\text{BZ}} \frac{d^2k}{2\pi} \text{Tr}[\Omega_{\vec{k}} \rho_{\vec{k}}(l)] \tag{4}$$

with the Berry curvature tensor $[\Omega_{\vec{k}}]_{vv'} = i\langle \nabla_{\vec{k}}\psi_{\vec{k}}^v| \times |\nabla_{\vec{k}}\psi_{\vec{k}}^{v'}\rangle_z = i(\langle \partial_{k_x}\psi_{\vec{k}}^v|\partial_{k_y}\psi_{\vec{k}}^{v'}\rangle - \langle \partial_{k_y}\psi_{\vec{k}}^v|\partial_{k_x}\psi_{\vec{k}}^{v'}\rangle)$ and l-th layer projector for the filled states $[\rho_{\vec{k}}(l)]_{vv'} = \langle \psi_{\vec{k}}^v|P_{\vec{k}}^{(l)}|\psi_{\vec{k}}^{v'}\rangle$. $P_{\vec{k}}^{(l)} = \sum_{j \in l} |\phi_j(\vec{k})\rangle\langle \phi_j(\vec{k})|$ defines the projector for all the states $|\phi_j(\vec{k})\rangle$ in the l-th layer, with $\sum_l P_{\vec{k}}^{(l)} = \mathbb{I}$. When taking the sum over all the layers in the crystal, $\sum_l \rho_{\vec{k}}(l) = \mathbb{I}$ and we arrive at the expected total anomalous Hall response

$$g_{xy} = \sum_l g_{xy}^{(l)} = \left(\frac{e^2}{h}\right) \int_{\text{BZ}} \frac{d^2k}{2\pi} \text{Tr}[\Omega_{\vec{k}}], \tag{5}$$

the finite temperature smearing simply introduces a Fermi function $n_F(\epsilon_{\vec{k},v})$ in the trace above for each band index v.

Section S5.4.2   Kernel polynomial method implementations

Most numerical simulations in the work are based on exact diagonalization method which limits the simulation scale. In order to reach larger thin film sizes we use the kernel polynomial method (KPM) (*25*) to compute the density of states (in the bulk and layer resolved) and the conductivity tensor. Our combined numerical approach and pipeline are shown schematically in Fig. **S11**.

Using the Wannier models derived from the ab-initio calculations as a tight binding Hamiltonian, the KPM approach can then be straightforwardly applied as an expansion of the relevant

23
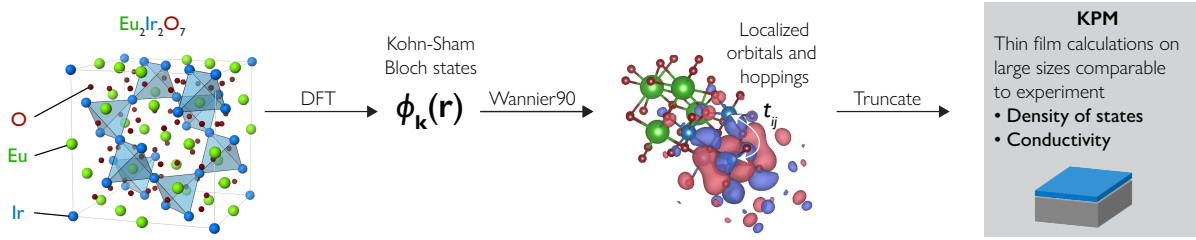
Fig. S11: A schematic of the numerical pipeline used starting from DFT to construct the Kohn-Sham orbitals that we map to a tight binding model through Wannier states. We then truncate the hopping matrix elements while retaining the relevant physics in order to reach mesoscopic thin film sizes. We make sure that on thin film sizes the truncation does not affect our results by comparing the KPM to exact diagonalization as in Fig. **S13**.

spectral quantity (i.e. conductivity tensor) in terms of orthogonal Chebyshev polynomials to an order N_C that controls the energy resolution of the calculation. The coefficients of the Chebyshev expansion can then be efficiently computed using matrix-vector operations avoiding the use of diagonalization. Using this approach allows us to reach on the order of 40 to 60 unit cells along the open boundary direction; while the in-plane extended dimensions can be treated using twisted periodic boundary condition allowing stable, efficient and vastly parallelizable sampling of the Brillouin zone.

The calculation of the conductivity tensor in KPM is based on the Kubo formula within linear response (*34*):

$$\sigma_{\alpha\beta}(\mu, T) = \frac{ie^2\hbar}{V} \int_{-\infty}^{\infty} d\epsilon f(\epsilon) \text{Tr}\left[v_\alpha \delta(\epsilon - H) v_\beta \frac{dG^+(\epsilon)}{d\epsilon} - v_\alpha \frac{dG^-(\epsilon)}{d\epsilon} v_\beta \delta(\epsilon - H)\right] \quad (6)$$

where V is the volume of the simulated lattice, $G^\pm$ is advanced (retarded) Green's function and f is the Fermi-Dirac distribution function at given temperature and chemical potential. The trace, which is the most computational demanding part for numerically evaluating the formula, can be well approximated using a stochastic evaluation (*25*). The anomalous Hall conductance (AHC) of the three-dimensional system is then given by $\text{AHC} = L_z \sigma_{xy}(\mu, T)$.

We take twisted periodic boundary condition along the two directions of the [111] plane
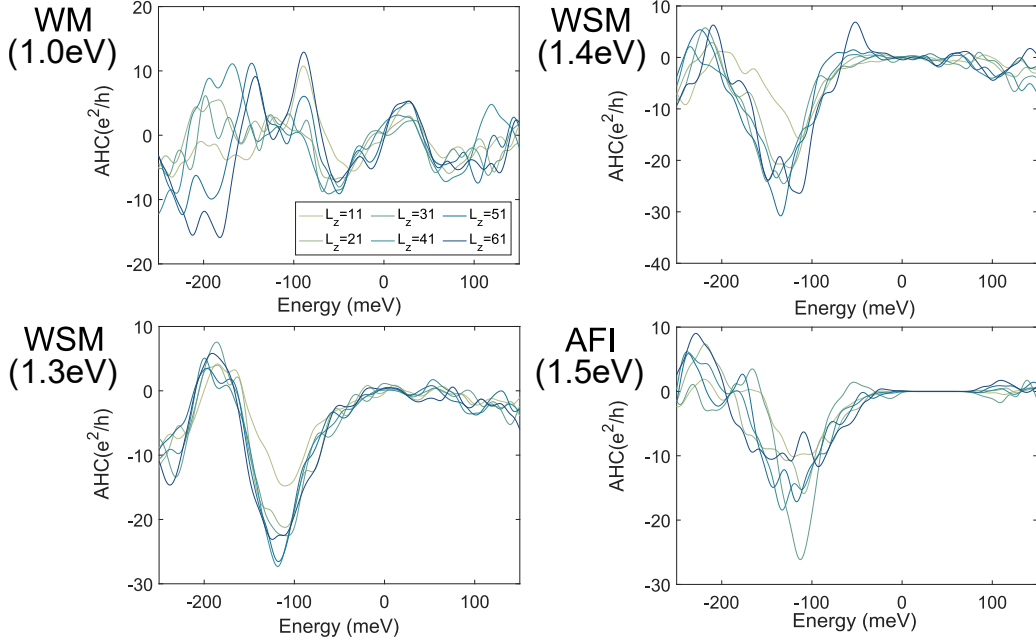
Fig. S12: The saturation of AHC as number of layer in the slab increases, with $U_{lr} = 1.0$eV (WM) , 1.3eV, 1.4eV (WSM) and $U_{lr} = 1.5$eV (AFI). The figures share legend, with darker color correspond to thicker slabs.

to effectively sample the momentum space of infinitely extended layers. The twist is applied through a factor of $e^{-i\vec{\theta}\cdot\vec{n}}$, where $\theta \in [0, 2\pi)$ is randomly picked for each sample, and $\vec{n}$ is the position of each operator in terms of primitive vectors. The lattice size on these dimensions only affects the number of random samples it takes for convergence. The perpendicular directions can have similar twisted periodic boundary condition to simulate bulk physics; while the slab geometry can be achieved with open boundary condition along this direction. Larger lattice size needs fewer sampling for the algorithm to converge, making it ideal for simulating slab width up to ~ 50 layers or above. The Hall conductance (as $\sigma_{xy}L_z$) shows saturation as the number of layers increases (Fig.**S12**).

We compare the KPM and the exact diagonalizaiton on the truncated Wannier model showing good agreement in Fig. **S13** of the density of states and the AHC. As the precise form of the broadening in the two cases is not equivalent we do expect the observed slight deviations of the
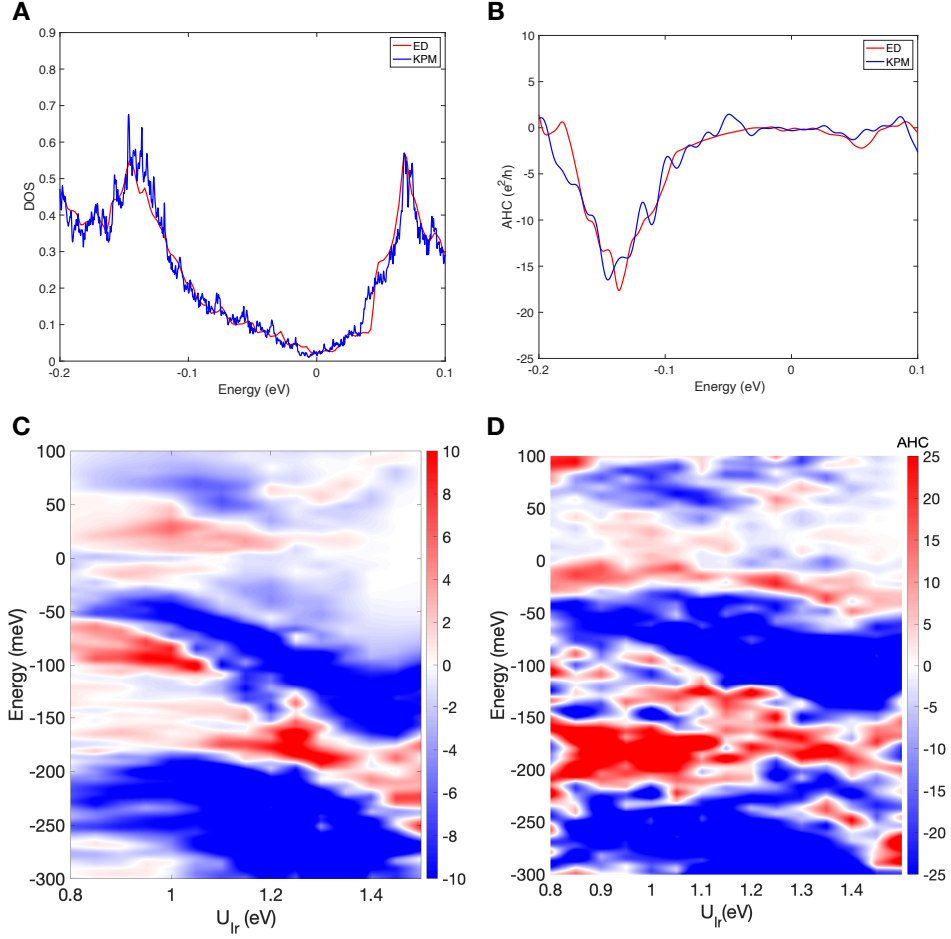
Fig. S13: Comparisons between exact diagonalization and kernel polynomial method. For a 11-layer slab at $U = 1.4\,\text{eV}$ (**A**) the slab density of states (**B**) the anomalous Hall conductance. (**C**) Anomalous Hall conductance map and the dependence on the U_{Ir} and energy using exact diagonalization method with a 11-layer slab (**C**) and the KPM implementation with much larger 41-layer slab in (**D**).

curves (e.g. the KPM resolves finer features in the density of states and AHC). The KPM allows us to directly explore much larger slabs then we can with exact diagonalization demonstrating that our map of the AHC shown in the main text with $L_z = 11$ layers remains qualitatively consistent with results at much larger slab sizes. In Fig. **S14** we show the density of states and longitudinal conductivity on larger slabs for various values of U_{Ir} across the phase diagram of the bulk model exploring the WM, the WSM, and the AFI. These results show the semimetallic
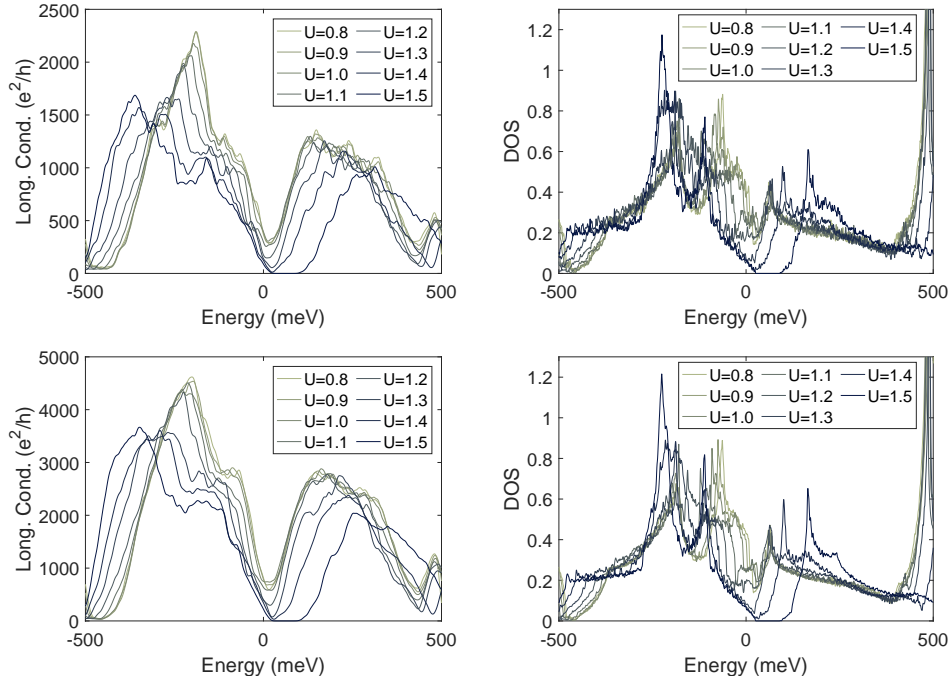
Fig. S14: Longitudinal conductance and density of states calculated using KPM method, at $U = 1.4$ eV with slab geometry of 21 (top row) and 41 (bottom row) layers. The darker curves correspond to larger U value. $U > 1.45eV$ correspond to the AFI phase with a clear gap and $U < 1.05$ is WM phase with finite density of state at the Fermi energy of Weyl nodes.

nature of the WSM regime is confined to a narrow range of U due to a very small (momentum dependent) gap away from the Weyl point.

Section S5.5   Further remarks on first principles modeling

Here for simplicity of the modeling, we ignore the complications near the surface and the slab model construction here relies only on the bulk Hamiltonian information. In reality, the various surface effects such as surface reconstruction for the crystal, dangling atomic bonds, charge transferring or redistribution with the substrate could introduce corrections to the above slab model. In principle, one could incorporate these effects by simulating a smaller slab within full DFT treatment and extracting the relevant information near the actual surface. These corrections

can be then added to the slab model to further improve the predictions. In the experiment, foreign atoms could be absorbed near the surface, or the additional interactions with the supporting substrate, which further complicate the modeling. We leave these considerations to the future studies, in conjunction with more elaborated experimental probes to examine the inter-facial properties near the substrate.

Section S6 Further First-principles electronic structure results

Section S6.1 Open versus periodic boundary conditions for the finite slabs

Previously, we have identified a non-zero AHC from the slab geometry with a finite extent in the stacking direction. From the symmetry perspective, this breaks the cubic symmetry of the crystal and allows for non-zero anomalous Hall responses in the basal plane. On the other hand, one could also employ the periodic boundary condition in the $[111]$ direction with (finite) L_z layers as well by artificially connecting the two terminating surfaces in the open boundary. This periodic structure breaks the cubic symmetry as well and for small L_z the non-zero AHE is also expected (*30*). In contrast to the open boundary slab, there are no terminating surfaces in the periodic slab.

On way to understand the non-zero AHE in the periodic slab is to start with the full 3D BZ. The periodic boundary condition can be viewed as the momentum discrete quantization along the 111 direction. As the result, one only samples discrete k points rather than continuously along this direction. To have the perfect cancellation in the 3D cubic lattice, it requires the full continuous integration of the Berry curvature at all momentum states. However, the momentum sampling here due to quantization creates a bias in the summation of the Berry curvature which leads to the non-zero AHE response in the basal plane. (In other words, this momentum quantization along $[111]$ direction is not compatible with the cubic symmetry of the crystal.) To demonstrate this effect, we consider a thin slab with $N = 6$, and the AHC responses are shown in Fig.**S15 A**. The results show that for a small, finite N, the AHC response from open or periodic boundary conditions can be comparable. The Berry curvature maps for both boundary conditions are shown in Fig.**S15**(B,C). One observation is that, the Berry curvature maps of the open boundary case contains features from the periodic boundary slab (smoother features of

the quantum well states from the quantization of bulk-like states). In addition, there are also identifiable surface features. As the finite size L_z along the periodic 111 direction increases, the non-zero AHE response must go to zero in the 3D bulk limit.
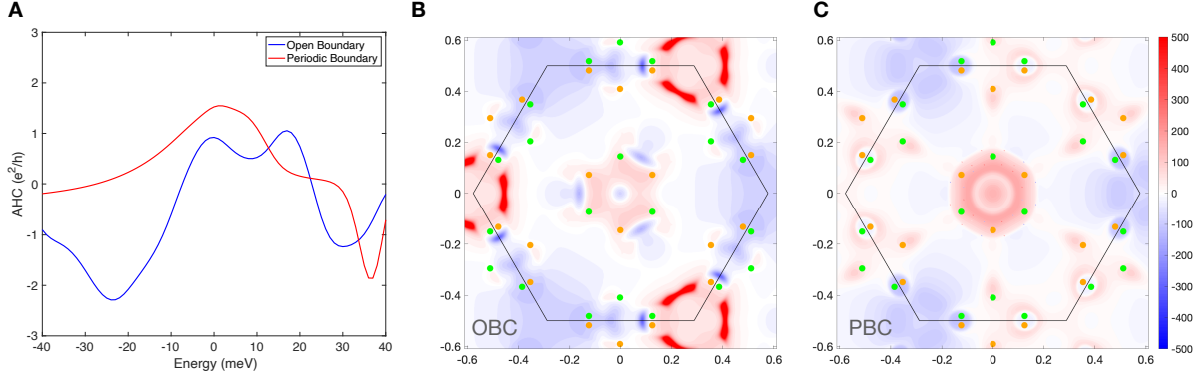

Fig. S15: The open boundary condition versus periodic boundary condition for a 6-layer slab at $U = 1.2$ eV. **(A)** The computed total anomalous Hall conductance with these two boundary conditions. The anomalous Hall response at Fermi level $E = 0$ can be decomposed into Berry curvature maps with **(B)** open boundary condition with two terminating surfaces and **(C)** periodic boundary condition.

For the measurement performed on the thin film fabricated (with $N \sim 50$), the AHC contribution is likely two-fold, which include both the surface states (the Fermi arcs, specifically, in the WSM phase), and the bulk-like states near the surface quantized by the finite thickness, similar to the quantum well states. In the layered resolved AHE contribution, we can see the dominant sources mostly from near the surface, compared to the middle region.

Section S6.2   Additional results in the Weyl metal phase (WM) with 8 Weyl nodes: bulk and thin film geometries

In the DFT+U phase diagram, the Weyl metal phase (WM) appears in $U_{c1} < U < U_{c2}$ regime. Within this parameter region, we find 8 Weyl nodes which form a cubic cage around the Γ point(Fig.**S16**A). In contrast with the WSM phase with 24 Weyl nodes, the Weyl points in WM coexist with additional parasitic metallic bands in the electronic spectrum. As shown in

A

B bulk projection

C triangle termination

D kagome termination
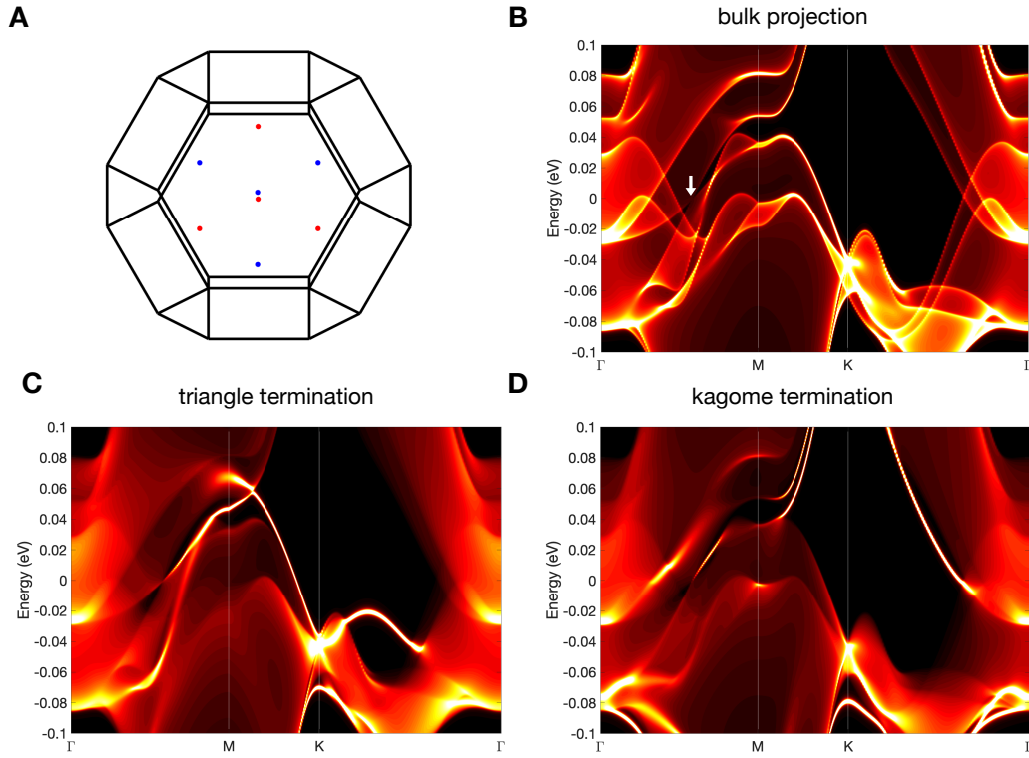
Fig. S16: Weyl metal (WM) phase at U = 1.0 eV **(A)** The locations of 8 Weyl nodes in the 3D bulk BZ. The red/blue color indicates opposite chiralities of the Weyl nodes. The spectral plot in a semi-infinite geometry can be computed from iterative Green's function method. In the projected 2D surface BZ perpendicular to the 111 direction, such spectral functions along $\Gamma - M - K - \Gamma$ can be derived for **(B)** deep bulk region which shows a faint signature for the Weyl node (white arrow) along $\Gamma - M$ **(C)** triangle lattice termination surface **(D)** kagome lattice termination surface.

Figs. **S14** and **S16**B-D the semi-metallic properties in the spectrum and transport are masked in the WM phase and gapped in the AFI phase. In Fig.**S17**, we show the momentum-resolved spectral function and Berry curvature maps of the 11-layer thin film, and their spatial projections into the surface and middle regions of the slab, at the Fermi level. This demonstrates that the non-trivial fluctuations of the AHC survive in the WM phase, but it is expected be a much more metallic system then the WSM regime.
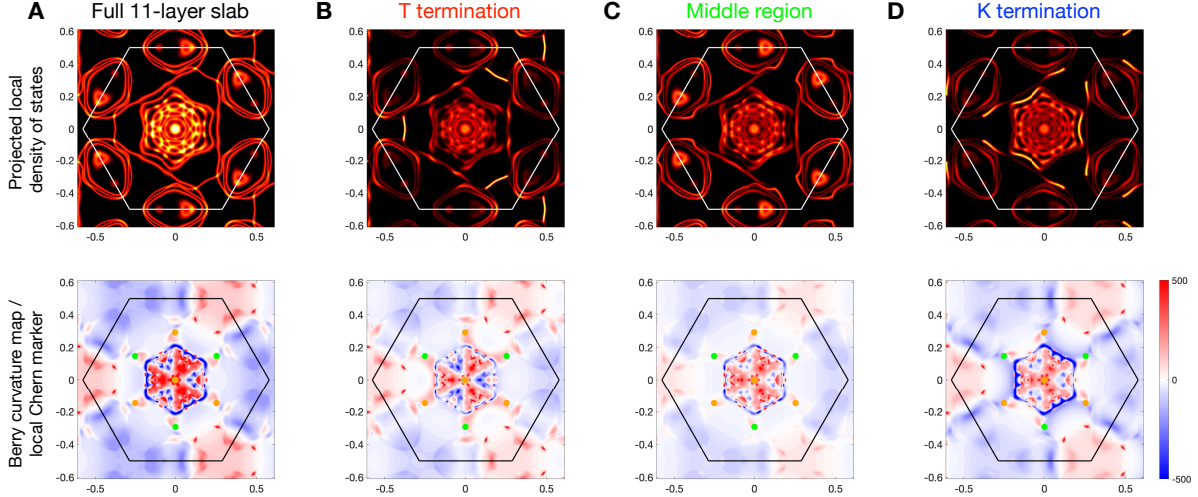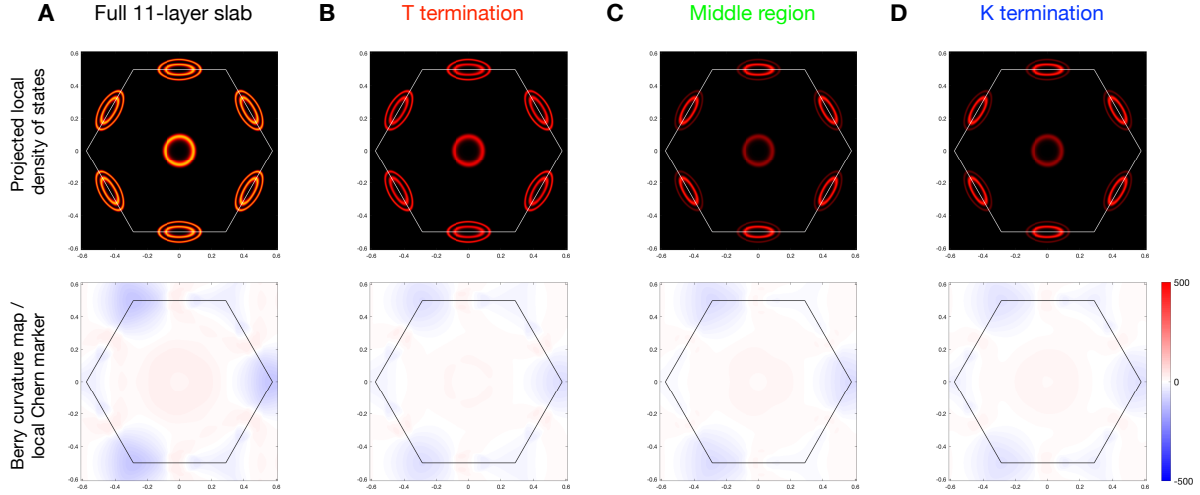
Fig. S17: **(A)** The maps of DOS and Berry curvatures at the Fermi level in a 11-layer slab at U=1.0 eV (WM phase) With wavefunction projections and local Chern markers, the contributions are further decomposed into **(B)** triangle termination **(C)** middle region **(D)** kagome termination regions.

Section S6.3   Thin film slabs in anti-ferromagnetic insulator phase (AFI)

In the DFT+U phase diagram, the anti-ferromagnetic insulator phase (AFI) can be stabilized at large U_{Ir} values ($U_{\text{Ir}} > 1.45$ eV) on top of AIAO magnetic ordering. In terms of electronic structure, this transition from WSM phase happens when the 24 Weyl nodes collide and annihilate at the BZ boundary. This leaves the bands near the Fermi level gapped.

Within the AFI phase, time reversal symmetry is still broken and in principle, non-zero AHE responses are to be expected in the finite slab. Within the gap, our simulation shows the trivial insulating behavior with vanishing AHC and Chern number. When the thin film slab is doped, the AHC could pick up non-zero Berry curvature distributions. How is the response compared to the WSM phase? Intuitively, Weyl points in WSM and WM are quite singular in the electronic structure as sources and sinks of the Berry curvature, and we expect a much smoother Berry curvature distribution in the AFI phase as these singular sources/sinks annihilate. In Fig.**S18**, we computed the AHE response and DOS map for 11-layer slabs with parameters in the AFI

Fig. S18: The maps of DOS and Berry curvatures at the E = -20 meV in a **(A)** 11-layer slab at U=1.5 eV (AFI phase) with wavefunction projections and local Chern markers, the contributions are further decomposed into **(B)** triangle termination **(C)** middle region **(D)** kagome termination regions.

phase. Despite a non-zero AHE response, in the AFI regime it is greatly reduced near the Fermi level. The distribution of the Berry curvature is also much smoother than in the WSM phase, as sources and sinks of Berry curvature (i.e. Weyl points) are removed from the spectrum. For the parameter estimation in the experiment, the AHC response near the Fermi level within AFI phase is much reduced. To reach order e^2/h AHC response, one has to substantially dope the system away from the Fermi level by around 100 meV. Hence we argue that, it is more plausible for the Weyl phase (WM or WSM) compared to doped AFI.

Section S6.4 Termination surface effects on anomalous Hall conductance

For the simulations, we have so far considered the slab geometry with one triangle termination surface on one side, and one kagome termination surface on the other side. This geometry retains the stoichiometry and vanishing net magnetic moment. Due to the inversion symmetry, it does not matter which termination surface is at the bottom or top side of the slab. Here

33
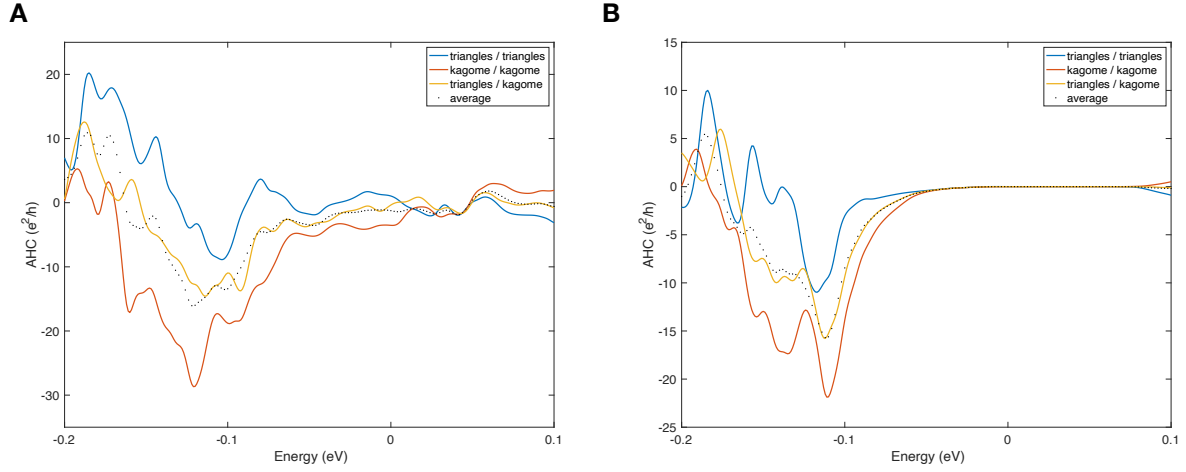
Fig. S19: Different arrangement of the bottom/top termination surfaces for the 11-layer slab at **(A)** U = 1.3 eV (WSM), **(B)** U = 1.5 eV (AFI). Each surface could be terminated at the triangle or the kagome lattice. The averages between the slab with both triangle and kagome lattices are also shown in black dotted lines. The slab with mixed triangles / kagome terminations are close to the average curves.

we would like to consider two alternative slab geometry, with both termination surfaces of the same lattice type. Both configurations give non-zero net magnetic moment in the slabs. The simulated anomalous Hall responses are in Fig.**S19**. Intuitively, the response for a triangle / kagome slab is roughly in between the triangle / triangle and kagome / kagome slabs of the same termination surfaces. The numerical average of the responses from slabs of the identical termination surfaces is also shown in black dotted lines, which is similar to the response from the balanced triangle / kagome slab. Within the AFI regime, the net magnetic moment does not lead to increase of anomalous Hall response within the band gap region. Therefore, the additional termination sheet added with net magnetic moment does not behave as the additional attachment of a 2D anomalous quantum Hall phase.

34
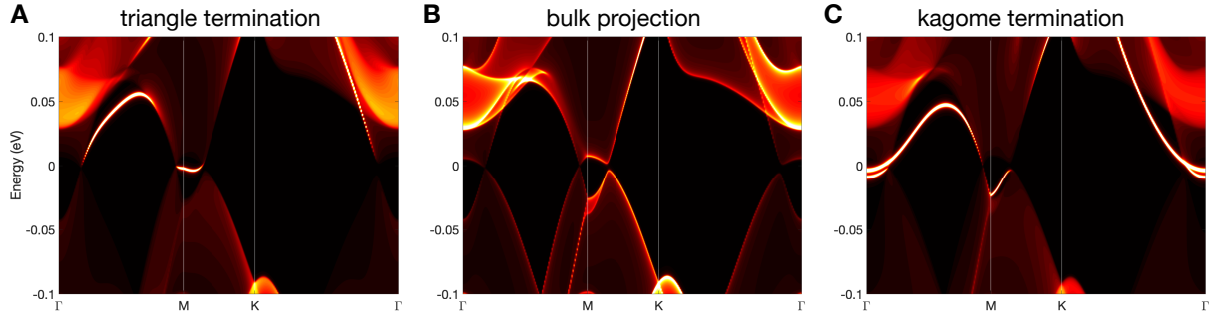
Fig. S20: The spectral plot in a semi-infinite geometry derived from iterative Green's function method. The surface terminated can be **(A)** triangle lattice or **(C)** kagome lattice, perpendicular (111) crystal axis. The momentum line cut is along Γ-M-K-Γ defined in 2D BZ. The spectral plot probed in the deep bulk region is shown in **(B)**. The parameter is at $U = 1.4$ eV with two projected Weyl points along Γ-M. The (Fermi arc) surface states can be seen in the surface projection.

Section S6.5   Semi-infinite geometry generalization

Practically, the finite slab geometry used above for investigating the surface effects would include additional hybridization between two terminating surfaces, which could be exacerbated when the slab thickness is not large enough. One trick to free us from this hybridization, if this is undesired, is to consider a semi-infinite geometry which has only one terminating surface. The modeling above can be straightforwardly applied in this setting. In this geometry, the iterative Green's function method (*24*) can be employed to efficiently simulate the self-energy operator from integrating out the infinite stacks of layers and hence the surface spectral function. This is used to illustrate the ideal surface local density of state properties in a single type of terminating surface normal to 111 axis as in Fig. **S20** and Fig.**S16**B-D.

References and Notes

1. X. Liu, F. Wen, E. Karapetrova, J.-W. Kim, P. J. Ryan, J. W. Freeland, M. Terilli, T.-C. Wu, M. Kareev, J. Chakhalian, *In-situ* fabrication and transport properties of (111) $Y_2Ir_2O_7$ epitaxial thin film. *Appl. Phys. Lett.* **117**, 041903 (2020).

2. J. Ishikawa, E. O'Farrell, S. Nakatsuji, Continuouos transition between antiferromagnetic insulator and paramagnetic metal in the pyrochlore iridate $Eu_2Ir_2O_7$. *Phys. Rev. B* **85**, 245109 (2012).

3. H. Sagayama, D. Uematsu, T. Arima, K. Sugimoto, J. Ishikawa, E. O'Farrell, S. Nakatsuji, Determination of long-range all-in-all-out ordering of Ir^{4+} moments in a pyrochlore iridate $Eu_2Ir_2O_7$ by resonant x-ray diffraction. *Phys. Rev. B* **87**, 100403(R) (2013).

4. D. Uematsu, H. Sagayama, T. Arima, J. Ishikawa, S. Nakatsuji, H. Takagi, M. Yoshida, J. Mizuki, K. Ishii, Large trigonal-field effect on spin-orbit coupled states in a pyrochlore iridate. *Phys. Rev. B* **92**, 094405 (2015).

5. J. P. Clancy, *et al.*, X-ray scattering study of pyrochlore iridates: Crystal structures, electronic, and magnetic excitations. *Phys. Rev. B* **94**, 024408 (2016).

6. B. T. Thole, P. Carra, F. Sette, G. van der Laan, X-ray circular dichroism as a probe of orbital magnetization. *Phys. Rev. Lett.* **68**, 1943-1946 (1992).

7. P. Carra, B. T. Thole, M. Altarlli, X. Wang, X-ray circular dichroism and local magnetic fields. *Phys. Rev. Lett.* **70**, 694-697 (1993).

8. C. T. Chen, Y. U. Idzerda, H.-J. Lin, N. V. Smith, G. Meigs, E. Chaban, G. H. Ho, E. Pellegrin, F. Sette, Experimental confirmation of the X-ray magnetic circular dichroism sum rules for iron and cobalt. *Phys. Rev. Lett.* **75**, 152-155 (1995).

9. J. Stöhr, Exploring the microscopic origin of magnetic anisotropies with X-ray magnetic circular dichroism (XMCD) spectroscopy. *J. Magn. Magn. Mater.* **200**, 470-487 (1999).

10. K. S. Pedersen, *et al.*, Iridates from the molecular side. *Nat. Commun.*, **7**, 12195 (2016).

11. M. C. Shapiro, S. C. Riggs, M. B. Stone, C. R. de la Cruz, S. Chi, A. A. Podlesnyak, I. R. Fisher, Structure and magnetic properties of the pyrochlore iridate $Y_2Ir_2O_7$. *Phys. Rev. B* **85**, 214434 (2012).

12. G. Kresse, J. Furthmüller, Efficient iterative schemes for ab initio total-energy calculations using a plane-wave basis set. *Phys. Rev. B* **54**, 11169 (1996).

13. G. Kresse, J. Furthmüller, Efficiency of ab-initio total energy calculations for metals and semiconductors using a plane-wave basis set. *Computational Materials Science* **6**, 15 (1996).

14. P. E. Blöchl, Projector augmented-wave method. *Phys. Rev. B* **50**, 17953 (1994).

15. J. P. Perdwe, K. Burke, M. Ernzerhof, Generalized Gradient Approximation Made Simple. *Phys. Rev. Lett.* **77**, 3865 (1996).

16. S. L. Dudarev, G. A. Botton, S. Y. Savrasov, C. J. Humphreys, A. P. Sutton, Electron-energy-loss spectra and the structural stability of nickel oxide: An LSDA+U study. *Phys. Rev. B* **57**, 1505 (1998).

17. N. Marzari, A. A. Mostofi, J. R. Yates, I. Souza, D. Vanderbilt, Maximally localized Wannier functions: Theory and applications. *Rev. Mod. Phys.* **84**, 1419 (2012).

18. A. A. Mostofi, J. R. Yates, G. Pizzi, Y. Lee, I. Souza, D. Vanderbilt, N. Marzari, An updated version of wannier90: A tool for obtaining maximally-localised Wannier functions. *Computer Physics Communications* **185**, 2309 (2014).

19. A. A. Mostofi, J. R. Yates, Y. Lee, I. Souza, D. Vanderbilt, N. Marzari, wannier90: A tool for obtaining maximally-localised Wannier functions. *Computer Physics Communications* **178**, 685 (2008).

20. Q. Wu, S. Zhang, H. Song, M. Troyer, A. A. Soluyanov, WannierTools : An open-source software package for novel topological materials. *Computer Physics Communications* **224**, 405 (2018).

21. T. Fukui, Y. Hatsugai, H. Suzuki, Chern Numbers in Discretized Brillouin Zone: Efficient Method of Computing (Spin) Hall Conductances. *Journal of the Physical Society of Japan* **74**, 1674 (2005).

22. M. D. Caio, G. Möller, N. R. Cooper, M. J. Bhaseen, Topological marker currents in Chern insulators *Nature Physics* **15**, 257 (2019).

23. N. Varnava, D. Vanderbilt, Surfaces of axion insulators. *Phys. Rev. B* **98**, 245117 (2018).

24. M. P. Lopez Sancho, J. M. Lopez Sancho, J. M. L. Sancho, J. Rubio, Highly convergent schemes for the calculation of bulk and surface Green functions. *J. Phys. F: Met. Phys.* **15**, 851 (1985).

25. A. Weiße, G. Wellein, A. Alvermann, H. Fehske, The kernel polynomial method. *Rev. Mod. Phys.* **78**, 275–306 (2006).

26. X. Wan, A. M. Turner, A. Vishwanath, S. Y. Savrasov, Topological semimetal and Fermi-arc surface states in the electronic structure of pyrochlore iridates. *Phys. Rev. B* **83**, 205101 (2011).

27. W. Witczak-Krempa, A. Go, and Y. B. Kim, Pyrochlore electrons under pressure, heat, and field: Shedding light on the iridates. *Phys. Rev. B* **87**, 155101 (2013).

28. W. Witczak-Krempa, Y. B. Kim, Topological and magnetic phases of interacting electrons in the pyrochlore iridates. *Phys. Rev. B* **85**, 045124 (2012).

29. A. Go, W. Witczak-Krempa, G. S. Jeon, K. Park, Y. B. Kim, Correlation Effects on 3D Topological Phases: From Bulk to Boundary. *Phys. Rev. Lett.* **109**, 066401 (2012).

30. B.-J. Yang, N. Nagaosa, Emergent topological phenomena in thin films of pyrochlore iridates. *Phys. Rev. Lett.* **112**, 246402 (2014).

31. H. Zhang, K. Haule, D. Vanderbilt, Metal-Insulator Transition and Topological Properties of Pyrochlore Iridates. *Phys. Rev. Lett.* **118** 026404 (2017).

32. R. Wang, A. Go, A. Millis. Weyl rings and enhanced susceptibilities in pyrochlore iridates: $k \cdot p$ analysis of cluster dynamical mean-field theory results. *Phys. Rev. B* **96**, 195158 (2017).

33. R. Wang, A. Go, A. J. Millis. Electron interactions, spin-orbit coupling, and intersite correlations in pyrochlore iridates.*Phys. Rev. B* **95**, 045133 (2017).

34. J. H. García, L. Covaci, T. Rappoport, G. Tatiana, Real-space calculation of the conductivity tensor for disordered topological matter. *Phys. Rev. Lett.* **114**, 116602 (2015).